

# Equivalent impedance and power analysis of monostable piezoelectric energy harvesters

Chunbo Lan<sup>1</sup>, Yabin Liao<sup>2</sup> , Guobiao Hu<sup>3</sup> and Lihua Tang<sup>3</sup>

## Abstract

Nonlinearity has been successfully introduced into piezoelectric energy harvesting for power performance enhancement and bandwidth enlargement. While a great deal of emphasis has been placed by researchers on the structural design and broadband effect, this article is motivated to investigate the maximum power of a representative type of nonlinear piezoelectric energy harvesters, that is, monostable piezoelectric energy harvester. An equivalent circuit is proposed to analytically study and explain system behaviors. The effect of nonlinearity is modeled as a nonlinear stiffness element mechanically and a nonlinear capacitive element electrically. Facilitated by the equivalent circuit, closed-form solutions of power limit and critical electromechanical coupling, that is, minimum coupling to reach the power limit, of monostable piezoelectric energy harvesters are obtained, which are used for a clear explanation of the system behavior. Several important conclusions have been drawn from the analytical analysis and validated by numerical simulations. First, given the same level of external excitation, the monostable piezoelectric energy harvester and its linear counterpart are subjected to the same power limit. Second, while the critical coupling of linear piezoelectric energy harvesters depends on the mechanical damping ratio only, it also depends on the vibration excitation and magnetic field for monostable piezoelectric energy harvesters, which can be used to adjust the power performance of the system.

## Keywords

energy harvesting, piezoelectric, nonlinear, monostable, impedance, maximum power, coupling, equivalent circuit

## 1. Introduction

In the past decade, piezoelectric energy harvester (PEH) has been extensively investigated to provide a sustainable power supply for small-scale devices (Liu et al., 2018; Tao et al., 2019; Wei and Jing, 2017), such as wireless sensors, medical implants, and wearable devices. Lots of strategies have been proposed by researchers (Daqaq et al., 2014; Erturk and Inman, 2011b; Liu et al., 2018) to improve the power output of PEHs, through either mechanical structural design or advanced circuit design. In the structural design, both linear and nonlinear energy harvesters were developed. The piezoelectric cantilever beam is one of the most representative linear PEHs, which has been well investigated (Erturk and Inman, 2011b). However, a linear PEH can only operate within a narrow bandwidth near the structural natural frequency to generate a power at a considerable level. In practical circumstances where the vibration sources are often featured with randomness and spread over a wide spectrum of frequency, the application of linear PEHs is significantly limited. As a solution to this issue, nonlinearities have been

introduced to the system (Daqaq et al., 2014) in order to broaden the operation bandwidth of linear PEHs. Based on the Duffing stiffness, monostable (Stanton et al., 2009), bistable (Cottone et al., 2009; Erturk and Inman, 2011a; McInners et al., 2008), and multi-stable (Zhou and Zuo, 2018) energy harvesters have been proposed. It has been revealed that these Duffing-type energy harvesters have much wider operation bandwidths than that of a conventional linear one if large-amplitude oscillations on the high-energy orbits can be

<sup>1</sup>State Key Laboratory of Mechanics and Control of Mechanical Structures, Nanjing University of Aeronautics and Astronautics, Nanjing, P.R. China

<sup>2</sup>Department of Mechanical Engineering Technology, Penn State Erie, The Behrend College, Erie, PA, USA

<sup>3</sup>Department of Mechanical Engineering, The University of Auckland, Auckland, New Zealand

## Corresponding author:

Yabin Liao, Department of Mechanical Engineering Technology, Penn State Erie, The Behrend College, 5101 Jordan Road, Burke Center 242, Erie, PA 16563, USA.

Email: Yabin.Liao@psu.edu

stimulated (Erturk and Inman, 2011a). Meanwhile, nonlinearities could also help improve the energy harvesting efficiency from random vibrations owing to the stochastic resonance (McInnes et al., 2008). In addition to Duffing-type PEHs, impact-based PEHs (Liu et al., 2012; Zhao and Yang, 2018), internal resonance-based PEHs (Chen and Jiang, 2015; Wu et al., 2018; Xu and Tang, 2017), magnetically coupled dual-beam PEHs (Lan et al., 2018b; Su et al., 2014), and nonlinear energy sink-based PEHs (Xiong et al., 2018) are other alternative solutions for broadband energy harvesting.

For linear PEHs, increasing the electromechanical coupling of the system is an effective way to improve the output power (Shu and Lien, 2006a). However, once the coupling reaches the critical level, any further increase of the coupling does not further enhance the power output, that is, the power saturates. Interestingly, regardless of the type of interface circuits, the saturated power level remains the same. Thus, there exists an overall maximum power (power limit) that can be attained for a given linear PEH. Although the power output characteristics of the harvester depend on the interface circuit, the harvested power is capped at this power limit. Since the power output is the most important parameter of an energy harvester, it is meaningful to determine the power limit and the critical coupling to reach the limit. Williams and Yates (1996) obtained an expression for the power limit of a linear PEH based on a model without considering the electromechanical coupling effect of PEH. The exact solution of the power limit for a linear PEH connected to a resistive interface circuit was derived by Liao and Sodano (2008). The maximum power of a linear PEH with RL circuit interface and RC circuit interface were studied by Renno et al. (2009) and Liao and Sodano (2009), respectively. Recently, Liao and Liang employed the equivalent impedance method (Liang and Liao, 2012) and the impedance matching technique (Liao and Liang, 2018) to analyze the power limit of a linear PEH shunted to more complicated interface circuits. They obtained the closed-form expression of the power limit based on representing the interface circuit (e.g. AC, DC, and SSHI (synchronized switch harvesting on inductor) as a generalized equivalent impedance. The power extraction behaviors of the interface circuits were clearly revealed, and the relationship between the internal impedance of the system and the external impedance of the circuit interface (Liao and Liang, 2019) was obtained.

For nonlinear PEHs, what is the maximum power that can be achieved, what is the condition to achieve the maximum power, and what is the connection between a nonlinear PEH to its linear counterpart? These major questions have yet been fully investigated.

Erturk and Inman (2011a) experimentally determined the optimal resistance of a bistable PEH under the weak electromechanical coupling condition. Stanton et al. (2012) analytically investigated the effect of resistance on the output power of a bistable PEH shunted to a resistive load by using the harmonic balance method (HBM). Lan et al. (2018a) further studied the effects of the load resistance on the power peak shifting and bandwidth variation of a monostable PEH connected to AC (resistive) and AC/DC (standard) interface circuits. It is revealed that for the monostable PEH, the increase of the resistance will result in a significant shift of power peak, which is quite different from a linear PEH. It is also noted that under the strong electromechanical coupling condition, there appear two peaks in the power spectrum of the monostable PEH, which is similar to a linear PEH. In the study of nonlinear PEHs, the performance comparison between nonlinear PEH and its linear counterpart is very common. Among these comparisons, one of the most representative works is presented by Stanton et al. (2009). In their work, it is found that the proposed monostable PEH has the advantages of bandwidth enlargement and power amplitude enhancement. However, since both linear and monostable PEHs were not optimized to reach the power limit, it is necessary to scrutinize the conclusion that the introduction of nonlinearity increases the efficiency of energy harvesting. For a fair comparison, the power limits under the optimal conditions need to be obtained for both linear and nonlinear PEHs.

To this end, this article is motivated to investigate the power limit and critical electromechanical coupling of a monostable PEH. The following content is organized as follows. In Section 2, the electromechanical modeling of monostable PEHs is briefly discussed, and the HBM is employed to analytically determine the harvested power. In Section 3, the expression of the power limit is derived based on the HBM. However, it has been found that, due to the existence of the nonlinear terms, the expressions of the optimal resistance and power limit are very complicated. Thus, it is very difficult to obtain an explicit solution of the power limit for a monostable PEH. To overcome this issue, an equivalent linearization method is proposed in Section 4 to approximate the nonlinear term in the governing system equation based on the HBM, and the equivalent circuit model of the monostable PEH is established. After that, in Section 5, the impedance matching concept is applied and the power limit and critical electromechanical coupling of the monostable PEH are clearly obtained. Moreover, the influences of the system parameters, such as base excitation and magnetic distance,

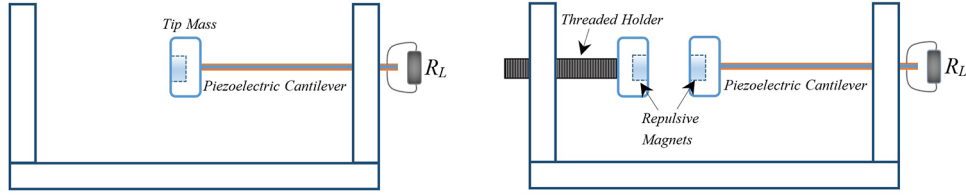


**Figure 1.** Schematics of (a) a linear PEH and (b) a monostable PEH.

on the power limit and the critical coupling are discussed. Finally, several important conclusions are summarized in Section 6.

## 2. System modeling and harmonic balance analysis

### 2.1. Modeling of a monostable PEH

Figure 1(a) and (b) shows the schematics of a linear and a monostable nonlinear PEHs, respectively. Their dynamic response characteristics and energy harvesting performance have been thoroughly investigated in the past few years. The linear PEH consists of a piezoelectric cantilever beam with a tip mass at the free end. The piezoelectric transducer is connected to an energy harvesting interface circuit. A purely resistive load is shown in the figure, which is the configuration of focus for this article. However, the approaches and results can be extended to other types of interface circuits as well. For the monostable PEH, another magnet is embedded in a threaded holder to provide a repulsive magnetic force. This threaded holder is adjustable and the magnetic force between the two magnets can be tuned by adjusting the distance between the magnets. The repulsive magnet system might be monostable or bistable, depending on the distance between the two magnets. For the linear PEH, the governing equations are given (Hagood et al., 1990) as

$$\begin{cases} M\ddot{w}(t) + C\dot{w}(t) + Kw(t) - \theta v_p(t) = Da(t) \\ \theta\dot{w}(t) + C_p\dot{v}_p(t) + i_p(t) = 0 \end{cases} \quad (1)$$

where  $w(t)$  is the temporal displacement,  $v_p(t)$  is the voltage across the piezoelectric patch,  $i_p(t)$  is the current through the piezoelectric patch, and the effective system parameters  $M$ ,  $C$ ,  $K$ ,  $\theta$ ,  $C_p$ ,  $a$ ,  $D$  are mass, damping, linear stiffness, nonlinear stiffness, electromechanical coupling, capacitance, acceleration of base excitation, and effective input mass, respectively. The overdot denotes the time derivative. It is noteworthy that similar modeling of linear PEHs have been developed by a lot of researchers (Yang et al., 2015, 2017, 2018). In this article, the experimentally validated single-mode model of the cantilevered beam energy harvester developed by Liao and Sodano (2008) is used, for which the effective system parameters have been obtained as

$$\begin{cases} M = \int_{V_s} \rho_s \varphi(x) \varphi(x) dV_s + \int_{V_p} \rho_p \varphi(x) \varphi(x) dV_p + M_t \\ K = \int_{V_s} y^2 \varphi''(x) c_s \varphi''(x) dV_s + \int_{V_p} y^2 \varphi''(x) c_p^E \varphi''(x) dV_p \\ \theta = - \int_{V_p} y \varphi''(x) e^T \psi(x) dV_p \\ C_p = \int_{V_p} \psi^T(y) \epsilon^S \psi(y) dV_p \\ C = \alpha M + \beta K \\ D = \int_{V_s} \rho_s \varphi(x) dV_s + \int_{V_p} \rho_p \varphi(x) dV_p + M_t \end{cases} \quad (2)$$

where  $\rho$  is the density,  $c$  is the modulus of elasticity,  $\epsilon$  is the dielectric constant,  $e$  is the piezoelectric coupling coefficient, and  $M_t$  is the mass of tip mass. The subscripts  $p$  and  $s$  represent the piezoelectric material and the substrate, respectively. The superscript,  $()^S$ , denotes the parameter was measured at a constant strain; superscript,  $()^T$ , denotes the parameter was measured at constant stress; and the superscript,  $()^E$ , indicates the parameter was measured at constant electric field.  $\varphi(x)$  is the vibration mode shape, and  $\psi(y)$  represents the electrical field over the thickness of the piezoelectric transducer, which is assumed to be constant. A proportional damping is added into the structure through the constants  $\alpha$  and  $\beta$ .  $a(t)$  is the excitation acceleration of the clamped end. The base motion excitation is converted to an equivalent external force given by the product  $Da(t)$ .

To accurately represent the nonlinear interaction force between the two repulsive magnets, the dipole-dipole model (Yung et al., 1998) is employed, which has been widely used in the modeling of monostable and bistable PEHs and whose high accuracy has been experimentally validated. The potential energy induced by the two magnets based on the dipole-dipole assumption is given as

$$U_m = - \frac{\bar{m}_A \bar{m}_B \bar{v}_A \bar{v}_B \mu_0}{4\pi} \left[ \frac{1}{(w^2 + D_0^2)^{1.5}} - \frac{3D_0^2}{(w^2 + D_0^2)^{2.5}} \right] \quad (3)$$

where  $\mu_0$  is the vacuum permeability,  $D_0$  is the initial center to center distance of between the two magnets,  $\bar{m}_A$  and  $\bar{m}_B$  are the magnitudes of magnetization vectors, and  $\bar{v}_A$  and  $\bar{v}_B$  are the volumes of the two magnets. The partial derivative of equation (3) with respect to

**Table 1.** System parameters of the monostable PEH.

Parameters	Value	Parameters	Value
Effective mass, $M$ (g)	8.2	Magnitudes of magnetization vectors, $\bar{m}_A, \bar{m}_B$ (A/m)	$0.955 \times 10^6$
Effective stiffness, $K$ (N/m)	138.6	Volume of magnets, $\bar{v}_A, \bar{v}_B$ (mm <sup>3</sup> )	$48\pi$
Damping ratio, $\zeta$	0.016	Vacuum permeability, $\mu_0$ (H/m)	$4\pi \times 10^{-7}$
Effective damping, $C$ (N s/m)	0.0354	Capacity of piezo patches, $C_p$ (pF)	87
Electromechanical coupling, $\theta$ (mV/N)	0.599	Resistance, $R_L$ (k $\Omega$ )	100
Effective input mass, $D$ (g)	8.2		

PEH: piezoelectric energy harvesting.

displacement  $w$  yields the restoring force between the two magnets

$$F_m = -\frac{\bar{m}_A \bar{m}_B \bar{v}_A \bar{v}_B \mu_0}{4\pi} \left[ -\frac{3w}{(w^2 + D_0^2)^{2.5}} + \frac{15wD_0^2}{(w^2 + D_0^2)^{3.5}} \right] \quad (4)$$

For the convenience to derive the analytical solution in the following study, the expression of magnetic force (equation (4)) is expanded by Taylor series at  $w = 0$ . Omitting the higher order terms, the nonlinear magnetic force can be approximated by

$$\begin{cases} F_m = -K_1 w + K_3 w^3 \\ K_1 = \frac{\bar{m}_A \bar{m}_B \bar{v}_A \bar{v}_B \mu_0}{4\pi} \frac{12}{D_0^5} \\ K_3 = \frac{\bar{m}_A \bar{m}_B \bar{v}_A \bar{v}_B \mu_0}{4\pi} \frac{45}{D_0^7} \end{cases} \quad (5)$$

Assuming that the effect of the magnetic force on the axial deformation of the cantilever beam is negligible and this magnetic force does not influence the linear components of the effective parameters of the cantilever PEH, combining equations (1) and (5) gives the governing equations of the monostable PEH (Cottone et al., 2009; Daqaq et al., 2014; Erturk and Inman, 2011a; Lan et al., 2018a; McInnes et al., 2008; Stanton et al., 2012)

$$\begin{cases} M\ddot{w}(t) + C\dot{w}(t) + Kw(t) - K_1 w(t) + K_3 w(t)^3 \\ -\theta v_p(t) = Da(t) \\ \theta \dot{w}(t) + C_p \dot{v}_p(t) + i_p(t) = 0 \end{cases} \quad (6)$$

## 2.2. Harmonic balance analysis

To obtain the approximate analytical solutions of this monostable PEH, the harmonic balance method (HBM) (Lan et al., 2018a; Stanton et al., 2012) has been employed and the detailed derivation is given in Appendix 1. The solutions of this monostable PEH are given as

$$r^2 \left[ \left( -\omega^2 M + K - K_1 + \frac{3}{4} K_3 r^2 + \frac{C_p (\theta R_L \omega)^2}{(C_p R_L \omega)^2 + 1} \right)^2 + \omega^2 \left( C + \frac{R_L \theta^2}{(C_p R_L \omega)^2 + 1} \right)^2 \right] = (DA)^2 \quad (7)$$

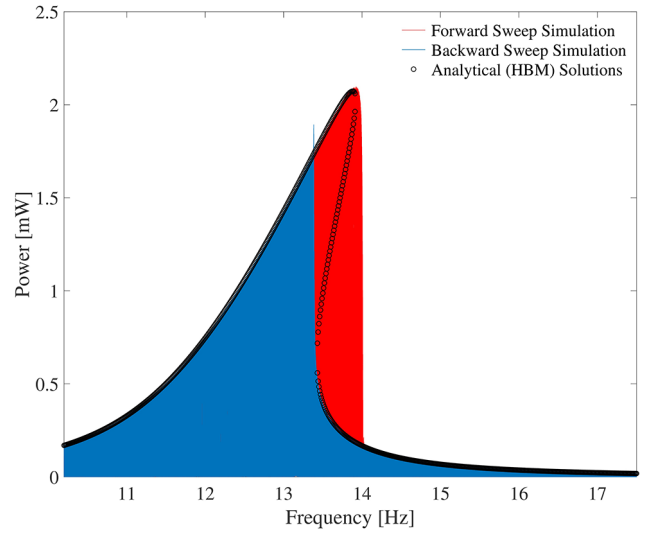


**Figure 2.** Comparison of the harvested power of the monostable PEH obtained by HBM and numerical simulation.

where  $r$  is the amplitude of displacement  $w$ ,  $A$  and  $\omega$  are the magnitude and frequency of the acceleration of the base motion, and  $D$  is the effective input mass. Additionally, the amplitude of output voltage and power have been obtained as

$$\begin{cases} V = \frac{\theta R_L \omega}{\sqrt{(C_p R_L \omega)^2 + 1}} r \\ P = \frac{(\theta \omega)^2 R_L}{(C_p R_L \omega)^2 + 1} r^2 \end{cases} \quad (8)$$

For the given parameters listed in Table 1, Figure 2 shows the analytical results obtained using equations (7) and (8). The numerical results obtained using the Runge–Kutta method are also provided for comparison and verification. Additional information used in the calculation include the following: the magnetic distance

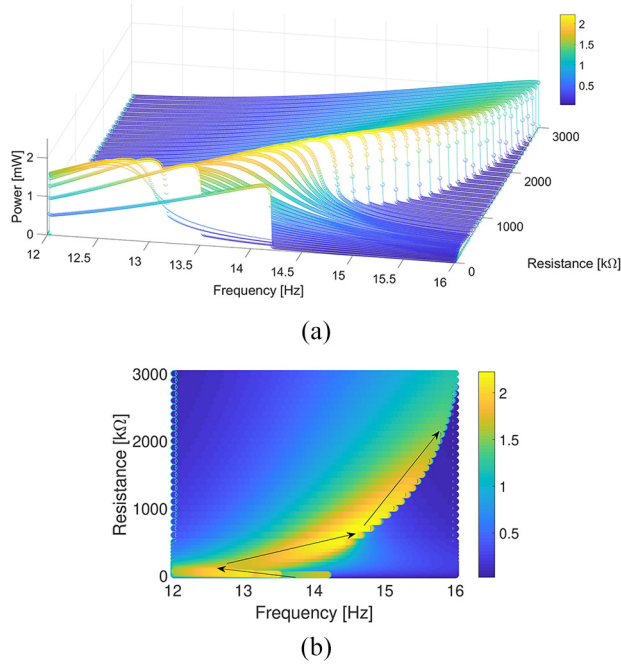


**Figure 3.** Frequency forward sweep responses of harvested power with varying resistance of a monostable PEH: (a) 3D waterfall maps and (b) top view graphic ( $\theta = 1200 \mu\text{V/N}$ ).

$D_0$  is 16 mm, the base acceleration  $A$  is  $2 \text{ m/s}^2$ , and the load resistance is  $R_L = 100 \text{ k}\Omega$ . From Figure 2, it can be seen that the analytical results derived by HBM agree very well with those from the numerical simulations. Moreover, the well-known “jump phenomenon” is observed from both the analytical and numerical results. In the forward sweep process, with the increase of  $\omega$ , the power first increases steadily then jumps abruptly down to a low energy orbit at a certain frequency after resonance. While in the backward sweep process, the power first increases slowly and then

suddenly jumps onto a much higher energy orbit. In addition, it is noted that the maximum power is achieved when  $\omega$  is close to the jump-down frequency.

### 3. Power characteristics and direct maximum power analysis of a monostable PEH

#### 3.1. Power characteristics

Similar to a linear PEH, the harvested power of a monostable PEH depends on the excitation frequency  $\omega$  and the electrical load  $R_L$ . This dependence is illustrated in the waterfall map in Figure 3, which was obtained through numerical simulations solving equation (6). In the simulations, the electromechanical coupling  $\theta = 1200 \mu\text{V/N}$  is chosen, with other parameters listed in Table 1. Since the maximum power occurs on the high-energy orbit of a monostable PEH (Figure 2), only the forward sweep responses are simulated and presented. The waterfall map consists of multiple power-versus-frequency curves with each curve obtained for a fixed  $R_L$ . With the increase of resistance from zero, the maximum power peak first moves toward a lower frequency and then returns and moves toward a higher frequency. This is different from a linear PEH, whose power peak monotonously moves to the right as the electrical load increases (Shu and Lien, 2006b). A detailed explanation of this phenomenon will be provided in Section 5.2.

To study the maximum power of a monostable PEH, the power peaks in Figure 3 are connected to show a power peak evolving orbit, as shown in Figure 4(a). Note that Figure 3 only shows the results for the electromechanical coupling  $\theta = 1200 \mu\text{V/N}$ , while Figure 4 includes results for other coupling levels to

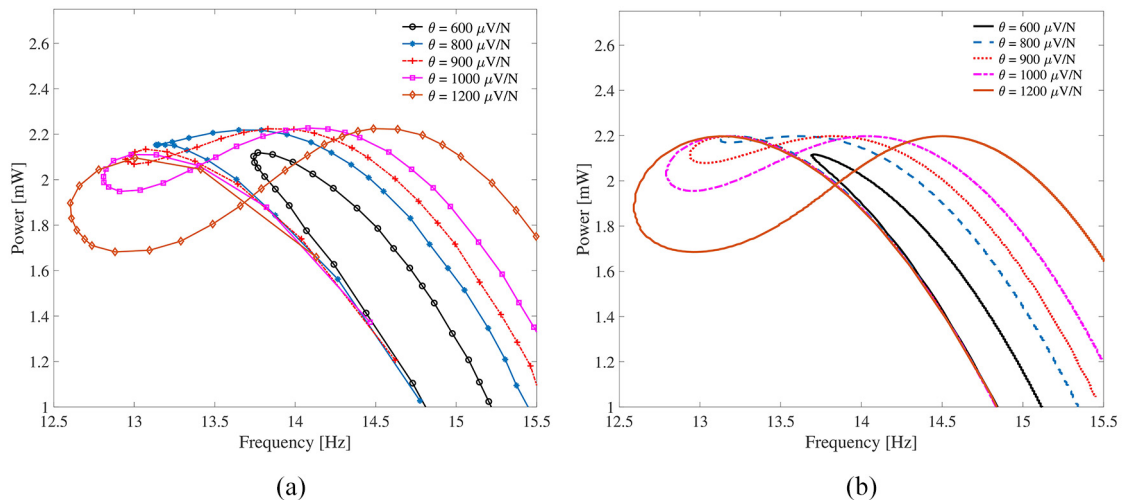


**Figure 4.** Power peak orbits of a monostable PEH for various coupling coefficient  $\theta$ : (a) numerical results from ODE simulations and (b) analytical results based on HBM.

**Table 2.** Comparison of numerical simulations and analytical solutions ( $\theta = 1200 \mu\text{N/V}$ ).

	Numerical simulation (ODE45)	Analytical solution (HBM)	Difference (%)
<b>Frequency of power peak 1 (Hz)</b>	13.07	13.12	0.38
<b>Frequency of power peak 2 (Hz)</b>	14.56	14.50	0.39
<b>Optimal resistance 1 (<math>\text{k}\Omega</math>)</b>	28	26	7.14
<b>Optimal resistance 2 (<math>\text{k}\Omega</math>)</b>	640	630	1.56
<b>Power limit (left) (mW)</b>	2.098	2.197	4.51
<b>Power limit (right) (mW)</b>	2.227	2.197	1.33

HBM: harmonic balance method.

demonstrate the effect of coupling on the power output. In addition, the analytical results based on HBM obtained from equations (7) and (8) are presented in Figure 4(b) for comparison. It appears that the effect of  $\theta$  on the harvested power of monostable PEHs has some similarity with that of linear PEHs (Lan et al., 2018a). Initially, the power level of the system increases as the coupling increases. The power peak orbit just has one overall peak. Once the coupling increases beyond a particular level, the overall maximum power saturates and there exist two overall peaks on the power peak orbit. After that, further increasing the coupling cannot further increase the power. In all, it appears that monostable PEHs also have a power limit phenomenon, similar to that of linear PEHs. This similarity and the difference between power behaviors of linear and monostable PEHs will be discussed further in Section 5.1.

A close inspection of Figure 4(a) and (b) reveals that overall the analytical results obtained based on the HBM method match the numerical simulation results. There do exist some minor discrepancy between them, which is expected because the analytical results are obtained using the HBM to approximate the original system (equation (6)). In the case of  $\theta = 1200 \mu\text{V/N}$ , the HBM results show that there are two power limit peaks at 13.07 and 14.56 Hz, respectively, and the harvested power is equal at 2.197 mW. The simulation results show two “power limit” peaks at about the same frequencies, with the power at the left peak equal to 2.098 mW (slightly underestimated) and at the right peak equal to 2.227 mW (slightly overestimated). Table 2 further compares the numerical simulation and HBM results in terms of optimal resistance, frequency of the power limit peaks, and the corresponding harvested power. The observed discrepancy could be induced by the effect of high-order harmonics ignored in HBM.

### 3.2. Direct maximum power analysis based on HBM

The numerical simulations and HBM analysis have shown interesting power behaviors of a monostable PEH, in particular, the power saturation phenomenon and the existence of a power limit. To investigate these, we first obtain the max power (or the power peak) of

the monostable PEH for a constant resistance. Note that in the second expression of equation (8), for a given resistance, the power is proportional to  $r^2$ . Thus, the problem of finding the maximum power for a given resistance becomes a problem of finding the maximum amplitude  $r_{\max}$ . For this purpose, equation (7) can be rewritten as

$$s_1 r^6 + s_2 r^4 + s_3 r^2 + s_4 = 0 \quad (9)$$

where the  $s$  coefficients in equation (9) are

$$\begin{cases} s_1 = \frac{9}{16} K_3^2 \\ s_2 = \frac{3}{2} K_3 \left( -\omega^2 M + K - K_1 + \frac{C_p (\theta R_L \omega)^2}{(C_p R_L \omega)^2 + 1} \right) \\ s_3 = \left( -\omega^2 M + K - K_1 + \frac{C_p (\theta R_L \omega)^2}{(C_p R_L \omega)^2 + 1} \right)^2 \\ \quad + \omega^2 \left( C + \frac{R_L \theta^2}{(C_p R_L \omega)^2 + 1} \right)^2 \\ s_4 = -(DA)^2 \end{cases} \quad (10)$$

Note that equation (9) is a cubic polynomial of  $r^2$ , which can have one or three real roots depending on the value of  $\omega$ . For a given  $R_L$ , the maximum amplitude of  $r^2$  occurs when the discriminant  $\Delta$  of the cubic equation (9) is equal to zero

$$\Delta = 18s_1 s_2 s_3 s_4 - 4s_2^3 s_4 + s_2^2 s_3^2 - 4s_1 s_3^3 - 27s_1^2 s_4^2 = 0 \quad (11)$$

and the associated maximum amplitude

$$r_{\max} = \sqrt{\frac{9s_1 s_4 - s_2 s_3}{2(s_2^2 - 3s_1 s_3)}} \quad (12)$$

By solving equation (11), the jump-up and jump-down frequencies of the monostable PEH can be obtained in terms of  $R_L$ . Substituting equation (12) and jump-down frequency (where the peak power occurs) into the second expression of equation (8) gives

$$P_{\max} = \frac{(\theta \omega)^2 R_L}{(C_p R_L \omega)^2 + 1} \left( \frac{9s_1 s_4 - s_2 s_3}{2(s_2^2 - 3s_1 s_3)} \right) \quad (13)$$



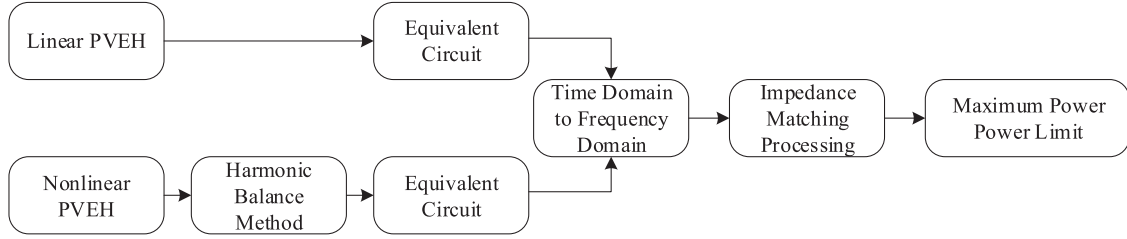


**Figure 5.** Technical routes of the impedance matching method for linear/nonlinear PEHs.

where  $P_{max}$  is the maximum power for a given  $R_L$ . Subsequently, by differentiating this power expression with respect to  $R_L$ , we can determine the optimal resistance and thus the power limit of the monostable PEH, which is the overall maximum power that can be possibly harvested. However, the mathematical expression of the solution  $\omega$  to equation (11) is very complex, leading to difficulties in obtaining explicit expressions of the maximum power and power limit. Certainly, numerical approaches could be employed, but the results cannot provide a clear insight into the effects of the system parameters on the maximum power and the power limit. In the following section, an equivalent impedance and circuit technique will be introduced and used to ascertain the power limit of a monostable PEH and its potential advantages over its linear counterpart.

#### 4. Equivalent impedance and circuit analysis

In the previous section, difficulties are encountered in the analysis of the maximum power and the power limit of the monostable PEH directly based on the electromechanically coupled system equations. The equivalent circuit method in conjunction with the impedance matching approach has been successfully applied into the study of the power characteristics and power limit of a linear PEH interfaced with various energy harvesting interface circuits in recent years (Liang and Liao, 2012; Liao and Liang, 2018, 2019). It has been shown by this method that there exists a power limit for a linear PEH regardless of the type of interface circuit. The vital idea of this method lies in the investigation of the relationship between the equivalent source impedance and external (equivalent) load impedance. The power limit is reached when the two impedances match.

This section presents an attempt to apply the same methodology to a monostable PEH, addressing a similar but more complicated problem due to nonlinearity. For linear PEHs, the methodology consists of three main steps: first, the equivalent circuit model is developed from the electromechanically coupled system equations using the analogy between the mechanical and electrical domains, converting mechanical components of the system into equivalent electrical elements.

Second, the established equivalent circuit is converted from the time domain to the frequency domain through Laplace transform and the elements are represented by impedances. Finally, the source and load impedances are defined, and the maximized power transfer occurs when the source impedance is conjugated with the load impedance, that is, impedance matching. It is worth mentioning that the equivalent circuit should be essentially linear for it to be directly converted into the frequency domain through Laplace transform. However, the monostable PEH has a nonlinear term in its governing equations, that is, equation (6). As a result, the methodology cannot be applied directly. To overcome this issue, an equivalent linearization method based on the harmonic balance analysis is proposed. After this linearization, the Laplace transform can then be applied to perform the time-to-frequency domain conversion. Finally, the impedance matching process can then be conducted to obtain the explicit expression of the power limit. The procedures of this methodology for analyzing linear and nonlinear PEHs are shown and compared in Figure 5. In this section, the establishment of the equivalent circuit model for linear PEHs is first briefly reviewed and then followed by that of the monostable PEH including the linearization method for handling the nonlinear term in the governing equation.

##### 4.1. Equivalent circuit model of linear PEHs

The detailed procedures for developing the equivalent circuit model of a linear PEH can be referred to in the study by Liao and Liang (2018). First, the electromechanical governing equations, equation (1), of a linear PEH can be rewritten as

$$\begin{aligned} \frac{M}{\theta^2} \frac{d}{dt} [-\theta \dot{w}(t)] + \frac{C}{\theta^2} [-\theta \dot{w}(t)] \\ + \frac{K}{\theta^2} \int [-\theta \dot{w}(t)] dt + v_p(t) = -\frac{D}{\theta} a(t) \end{aligned} \quad (14)$$

Define the equivalent source voltage and current as

$$v_{eq}(t) = -\frac{D}{\theta} a(t), \quad i_{eq} = -\theta \dot{w}(t) \quad (15)$$

Substituting the equivalent expressions back into equation (14) yields

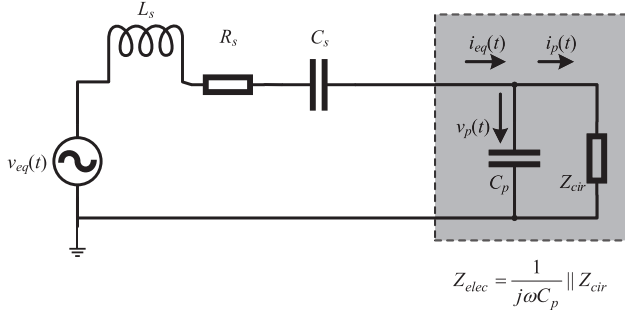


**Figure 6.** Equivalent circuit representation of a linear PEH.

$$v_{eq}(t) = \frac{M}{\theta^2} \dot{i}_{eq} + \frac{C}{\theta^2} i_{eq} + \frac{K}{\theta^2} \int i_{eq} dt + v_p(t) \quad (16)$$

where the equivalent electrical elements are related to the original mechanical elements as

$$L_s = \frac{M}{\theta^2}, R_s = \frac{C}{\theta^2}, C_s = \frac{\theta^2}{K} \quad (17)$$

In addition to the voltage relationships (equation (16)), the current relationship can be obtained by rewriting the second expression of equation (1) as

$$i_{eq}(t) = C_p \dot{v}_p(t) + i_p(t) \quad (18)$$

Based on the voltage relationship given in equation (16) and the current relationship given in equation (18), the equivalent circuit in Figure 6 is obtained, where  $Z_{cir}$  is the circuit impedance representing the energy harvesting interface circuit and  $Z_{elec}$  is defined as the electrical impedance as a combination of the intrinsic piezoelectric capacitance  $C_p$  and the circuit impedance  $Z_{cir}$ .

#### 4.2. Equivalent circuit model of monostable PEHs

In the case of a monostable PEH, the nonlinear term  $K_3[w(t)]^3$  in the first expression of equation (6) needs to be linearized before developing the equivalent circuit model. For this purpose, the HBM as detailed in Appendix 1 is applied

$$K_3[w(t)]^3 = K_3 \left[ (a_1^3 + a_1 b_1^2) \frac{3}{4} \sin(\omega t) - (a_1^3 - 3a_1 b_1^2) \frac{1}{4} \sin(3\omega t) + (b_1^3 + b_1 a_1^2) \frac{3}{4} \cos(\omega t) - (b_1^3 - 3b_1 a_1^2) \frac{1}{4} \sin(3\omega t) \right] \quad (19)$$

By neglecting the higher harmonics, the cubic term of  $w(t)$  can then be approximated as

$$K_3[w(t)]^3 \approx \frac{3}{4} K_3 |r|^2 w(t) \quad (20)$$

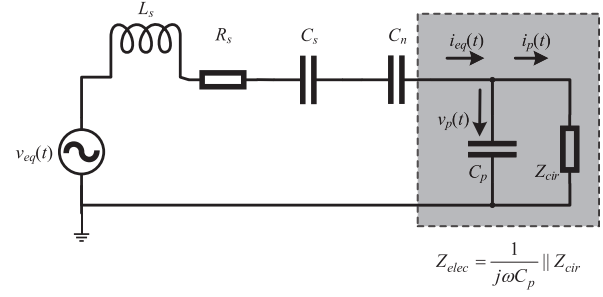


**Figure 7.** Equivalent circuit representation of a monostable PEH.

where  $|r| = \sqrt{a_1^2 + b_1^2}$  is the amplitude of displacement. Substituting this expression into governing equation (6) yields

$$\begin{cases} M\ddot{w}(t) + C\dot{w}(t) + Kw(t) - K_1 w(t) + \frac{3}{4} K_3 |r|^2 w(t) \\ - \theta v_p(t) = Da(t) \\ \theta \dot{w}(t) + C_p \dot{v}_p(t) + i_p(t) = 0 \end{cases} \quad (21)$$

Comparing equations (6) and (21) shows that the magnet-induced nonlinearity effectively introduces an equivalent stiffness into the linear system from a mechanical perspective

$$-K_1 + \frac{3}{4} K_3 |r|^2 \quad (22)$$

Note that this equivalent stiffness is not constant but  $r$ -dependent. Following the similar equivalent circuit modeling process for linear PEHs, the first expression of equation (21) is rewritten as

$$v_{eq}(t) = \frac{M}{\theta^2} \dot{i}_{eq} + \frac{C}{\theta^2} i_{eq} + \frac{K}{\theta^2} \int i_{eq} dt + \frac{-K_1 + \frac{3}{4} K_3 |r|^2}{\theta^2} \int i_{eq} dt + v_p(t) \quad (23)$$

With some algebraic manipulation, equation (23) can be rearranged into the form as

$$v_{eq}(t) = L_s \dot{i}_{eq} + R_s i_{eq} + \frac{\int i_{eq} dt}{C_s} + \frac{\int i_{eq} dt}{C_n} + v_p(t) \quad (24)$$

where the equivalent electrical elements are related to the original mechanical elements by

$$L_s = \frac{M}{\theta^2}, R_s = \frac{C}{\theta^2}, C_s = \frac{\theta^2}{K}, C_n = \frac{\theta^2}{-K_1 + \frac{3}{4} K_3 |r|^2} \quad (25)$$

Based on equation (24), the equivalent circuit model for the monostable PEH is obtained as shown in Figure 7. Note that the effect of the magnets is modeled



through the capacitor  $C_n$ , which connected in series with the equivalent source capacitor  $C_s$ .

## 5. Power characteristics of a monostable PEH

### 5.1. Impedance matching and power limit analysis

From the equivalent circuit in Figure 7, the overall equivalent impedance for the mechanical part of the system is

$$Z_{mech}(j\omega) = j\omega L_s + R_s + \frac{1}{j\omega C_s} + \frac{1}{j\omega C_n} \quad (26)$$

which consists of the three original source elements  $L_s$ ,  $R_s$ ,  $C_s$  associated with the linear PEH part of the system, and the nonlinear element  $C_n$  representing the effect of magnets. The electrical load impedance  $Z_L$  consists of the impedance from the piezoelectric capacitance  $C_p$  and the energy harvesting circuit impedance  $Z_{cir}$

$$Z_{elec}(j\omega) = \frac{1}{j\omega C_p} || Z_{cir} = \left( j\omega C_p + \frac{1}{Z_{cir}} \right)^{-1} \quad (27)$$

Consider the entire equivalent mechanical impedance in equation (26) as the source impedance, and the electrical impedance in equation (27) as the load impedance, that is

$$Z_S = Z_{mech}, Z_L = Z_{elec} \quad (28)$$

This yields a generic circuit schematic as shown in Figure 8, to which the concept of impedance matching can be applied.

The maximum power transfer or extraction occurs when the source impedance and load impedance are matched

$$Z_L = Z_S^* \quad (29)$$

where the asterisk symbol denotes complex conjugate. When the load impedance  $Z_L$  is matched to the source impedance  $Z_S$ , the power transferred to the load impedance can be obtained as

$$P_{\max} = \frac{V_{eq}^2 R_s}{4} \quad (30)$$

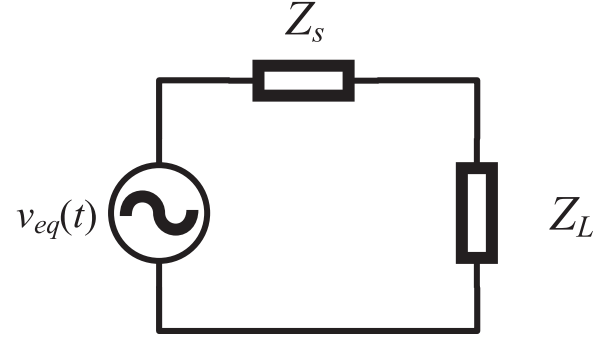


**Figure 8.** Schematic for impedance matching.

which could also be regarded as the maximum power could be extracted by the load impedance from the system, that is, power limit. Substituting the equivalent circuit parameters defined in equations (15) and (17) back into equation (30) yields the power limit

$$P_{\lim} = \frac{D^2 A^2}{4C} = \frac{D^2 A^2}{\sqrt{MK}} \frac{1}{8\zeta} \quad (31)$$

which, interestingly, turns out to be the same as that for linear PEHs (Brenes et al., 2020; Liao and Liang, 2018). This can be explained by comparing the equivalent circuits of linear and monostable PEHs shown in Figures 6 and 7. Electrically, adding the magnetic force to make the system monostable is equivalent to adding a nonlinear capacitor, that is,  $C_n$ , in series with the original source elements. Since the nonlinear capacitor is a reactive element, it is canceled by the reactive component of the matched load impedance when impedance matching occurs. As a result, the power limit only depends on the resistive component of the source impedance, which remains the same with or without the magnetic force.

To find the optimal impedance of the energy harvesting circuit for impedance matching, define the circuit impedance in the form

$$Z_{cir} = R_{cir} + jX_{cir} \quad (32)$$

Substituting it into equation (27) and applying impedance matching to equation (28) yield the optimal circuit impedance components in terms of the effective system parameters

$$\begin{cases} \bar{R}_{cir} = \frac{\theta^2 C}{[\theta^2 - C_p(\omega^2 M - K + K_1 - \frac{3}{4}K_3|r|^2)]^2 + C^2(\omega C_p)^2} \\ \bar{X}_{cir} = \frac{1}{\omega C_p} \frac{C_p(\omega^2 M - K + K_1 - \frac{3}{4}K_3|r|^2)[- \theta^2 + C_p(\omega^2 M - K + K_1 - \frac{3}{4}K_3|r|^2)] + C^2(\omega C_p)^2}{[\theta^2 - C_p(\omega^2 M - K + K_1 - \frac{3}{4}K_3|r|^2)]^2 + C^2(\omega C_p)^2} \end{cases} \quad (33)$$

Equation (33) gives the optimal circuit impedance that matches the source impedance to reach the power limit. However, due to physical constraints of the circuit or the configuration of the system, this optimal impedance might not be attainable. This will be further discussed in Section 5.3.

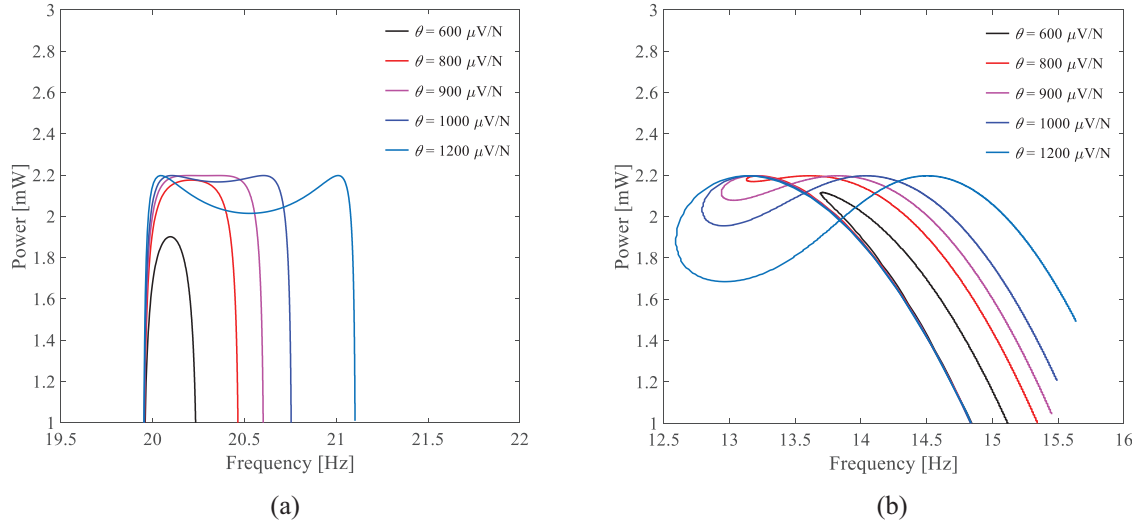


**Figure 9.** Power peak orbits for various electromechanical coupling: (a) linear PEH and (b) monostable PEH ( $A = 2 \text{ m/s}^2$ ).

## 5.2. Comparison and connection between linear and monostable PEHs

**5.2.1. Comparison of linear and monostable PEHs.** The theoretical analysis in the previous section shows that the linear and monostable PEHs have the same power limit. This is graphically illustrated in Figure 9, where the power peak orbits of linear and monostable PEHs are plotted for different electromechanical coupling. As explained in Section 3.1, each power peak point on the orbit is obtained by performing a forward frequency sweep under a given resistance and finding the peak power and associated frequency. Then the resistance is varied, resulting in a set of power peaks with each corresponding to a particular resistance. Connecting the power peaks results in the power peak orbits shown in Figure 9. The most important and noticeable relationship is that the power limit is the same for both at 2.197 mW. In addition, though the power peak orbits of monostable PEHs are much more complex than that of linear PEHs due to the effect of nonlinearity, there are a few similarities between them. For both, the overall power level increases with the increase of the coupling initially. Then, it saturates after the coupling reaches a critical level and the power limit is reached at two locations.

On the contrary, there are also differences in the power behaviors. Most noticeably, the power peaks of linear PEHs monotonously move to the right with the increase of resistance. This is due to the increase of the effective stiffness of the system induced by electromechanical coupling (Liao and Liang, 2018). However, for monostable PEHs, the power peak moves to the left initially and then to the right as the resistance increases. This can be explained using the structural effects, that

is, stiffness and damping, of energy harvesting (Lan et al., 2018a). From equation (7), the effective stiffness of the monostable system can be defined as

$$K_{\text{eff}} = K - K_1 + \frac{3}{4}K_3r^2 + \frac{C_p(\theta R_L\omega)^2}{(C_pR_L\omega)^2 + 1} \quad (34)$$

where the first term on the right is the short-circuit stiffness of the linear PEH part of the system, which is a constant. The last term represents the additional stiffness due to piezoelectric coupling. It increases monotonously with the increase of resistance and leads to a power peak shift from the short-circuit to open-circuit natural frequencies for linear PEHs. The second and third terms are the nonlinear stiffness contribution from the magnet mechanism, which depends on the vibration response of the system, that is,  $r$ . The short-circuit stiffness is a constant and usually the additional piezoelectric stiffness is not much compared to the short-circuit stiffness. Therefore, the change in the overall effective stiffness is mostly caused by the nonlinear stiffness. When the resistance is very small, the induced electrical damping is low and the structural response represented by  $r$  is large. As a result, the nonlinear stiffness is large. As the resistance increases, the induced damping also increases and reaches its maximum at a medium resistance. At this moment, the structural response and the nonlinear stiffness are minimized. Further increase of resistance after this optimal point reduces the damping and the structural response becomes larger again. As a result, the nonlinear stiffness increases. In all, as the resistance increases, the nonlinear stiffness initially decreases, reaches its minimum, and then increases after that. Consequently, the power peak first moves to a lower frequency and then returns and moves to the

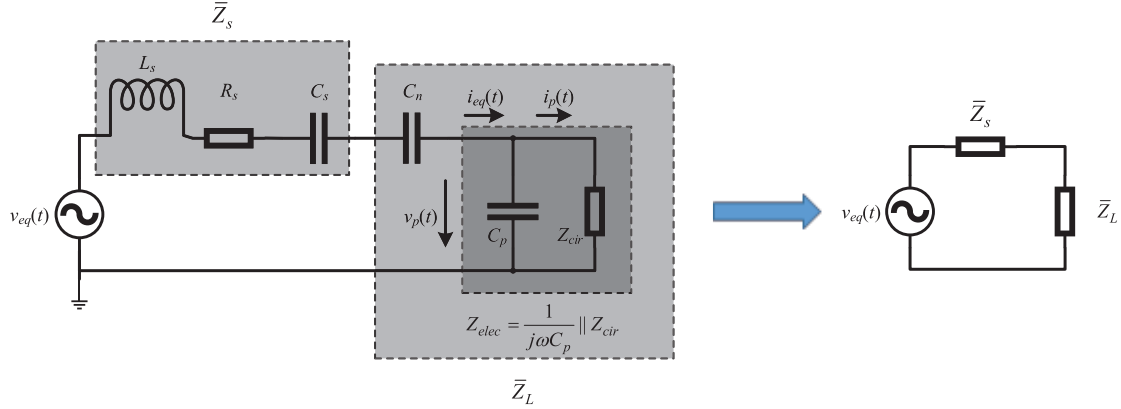


**Figure 10.** Modified schematic for impedance matching.

higher frequency. This “variability” of the nonlinear stiffness makes it possible for the effective natural frequency of the system to move in a much wider frequency range, an attractive feature for broadband energy harvesting. In addition to the more complex behavior of the power peak orbits of monostable PEHs, the orbits have an overall shift to lower frequencies compared to those of linear PEHs. Physically, this is because that the structural response is “amplified” by the additional repulsive force between the magnets. As a result, the system becomes “softer” and the effective natural frequency decreases. Mathematically, this is because that the nonlinear stiffness in equation (34) is negative for small vibration excitation, leading to a decreased overall effective stiffness.

Finally, though the overall effect of electromechanical coupling on the power is similar, there do exist some differences in the exact extent of this effect. For example, when  $\theta = 800 \mu\text{V/N}$ , the monostable PEH has already reached the power limit while the linear PEH still has one power peak. In other words, when  $A = 2 \text{ m/s}^2$ , the critical electromechanical coupling of monostable PEH is smaller than that of linear PEH. However, the critical electromechanical coefficient of monostable harvester depends on the base acceleration level. More specifically, it might be true for low acceleration level, such as  $A = 2 \text{ m/s}^2$ , but the critical coupling could become greater than that of linear PEH at high excitation level. A detailed discussion of the relationship between coupling and excitation will be provided in Section 5.3.

**5.2.2. Connection between linear and monostable PEHs.** In Section 5.1 and Figure 7, the nonlinear magnetic effect of a monostable PEH is treated as a component of the mechanical source impedance. A modified treatment is illustrated in Figure 10, which considers the magnetic effect as a part of the external electrical load impedance. Mathematically, this modified model has the source

impedance the same as that of a linear PEH (Liao and Liang, 2018) (refer to Figure 6)

$$\bar{Z}_s = j\omega L_s + R_s + \frac{1}{j\omega C_s} = \frac{C}{\theta^2} + j\frac{1}{\omega\theta^2} [\omega^2 M - K] \quad (35)$$

while the magnet impedance  $Z_n$  is included as a part of the modified load impedance

$$\begin{aligned} \bar{Z}_L = Z_L + Z_n = & \frac{R_{cir} + j(-\omega C_p X_{cir}^2 - \omega C_p R_{cir}^2 + X_{cir})}{(-\omega C_p X_{cir} + 1)^2 + (\omega C_p R_{cir})^2} \\ & + j\frac{1}{\omega\theta^2} \left( K_1 - \frac{3}{4} K_3 |r|^2 \right) \end{aligned} \quad (36)$$

It can be shown that applying impedance matching to these two impedances yields the same power limit expression as given in equation (31) and the optimal circuit impedance components given in equation (33).

Comparing Figures 6 and 10 offers a valuable perspective on the similarities in the power behavior exhibited by linear and monostable PEHs and the connection between them. Adding magnets to a linear PEH to make it monostable is equivalent to adding a nonlinear capacitor into the electrical energy harvesting interface circuit of the linear PEH. As discussed in Liao and Liang (2018), as long as the source impedance remains the same, the power limit is the same regardless of the circuit interface. The effect of magnets is equivalent to providing an auxiliary electrical element, that is, the nonlinear capacitor  $C_n$ , to change or tune the electrical impedance of the original linear PEH. The capacitance of this nonlinear capacitor is negative when the structural response is low, and positive when the response is large.

The relationship between the source and load impedances has a significant effect on the power behavior of a system. For linear harvesters, the relationship can be graphically presented through an impedance plot of the “matched” and “tuning” impedances (Liao, 2019; Liao

and Liang, 2018). The matched electrical impedance is defined as the complex conjugate of the source impedance for impedance matching

$$\bar{Z}_m = \frac{C}{\theta^2} - j \frac{1}{\omega \theta^2} [\omega^2 M - K] \quad (37)$$

The tuning impedance is essentially the electrical load impedance given in equation (36). The word “tuning” is used here to emphasize the change of this load impedance as the parameters change. For monostable harvesters with a resistive interface circuit, the expression of this tuning load impedance can be obtained from equation (36) as

$$\bar{Z}_L = \frac{R}{1 + (\omega C_p R)^2} + j \left[ \frac{1}{\omega \theta^2} \left( K_1 - \frac{3}{4} K_3 |r|^2 \right) - \frac{\omega C_p R^2}{1 + (\omega C_p R)^2} \right] \quad (38)$$

To reach the power limit, the tuning electrical impedance needs to be equal to the matched impedance, which may or may not be possible depending on the coupling of the system. Note that the tuning impedance of its linear counterpart can be obtained easily by setting  $K_1$  and  $K_2$  to be zero in equation (38).

The impedance plot has been shown to be a useful tool to gain insights and better understanding of power behavior of linear harvesters, for example, the relationships between power and load resistance, and between power limit and electromechanical coupling. It is natural to attempt the same idea on monostable harvesters. However, the impedance plot has a couple of important differences from that of linear harvesters. First, the tuning impedance as shown in equation (38) depends on the level of response due to nonlinearity, while its linear counterpart does not. This will be illustrated and discussed further in the next section. Second, the impedance plot does not plot the impedance  $Z$  directly, but in its dimensionless form  $\omega C_p Z$ . For linear harvesters, the benefit of this form is that the tuning effects of frequency  $\omega$  and load resistance  $R$ , which could be applied independently, are effectively combined through the “global” variable  $\omega C_p R$ . Varying this global variable results in a tuning curve on the impedance plot. Regardless how the system is tuned through  $\omega$  or  $R$ , or both, the corresponding impedance point falls on this curve. However, it can be seen from equation (38) that the dimensionless form  $\omega C_p Z$  shall not be able to reduce the two independent variables  $\omega$  or  $R$  into a single global variable  $\omega C_p R$  anymore because of the response term  $r^2$  (refer to equation (7)). Graphically, this means that the tuning impedance does not follow a single curve anymore but its location becomes scattered over the impedance plane.

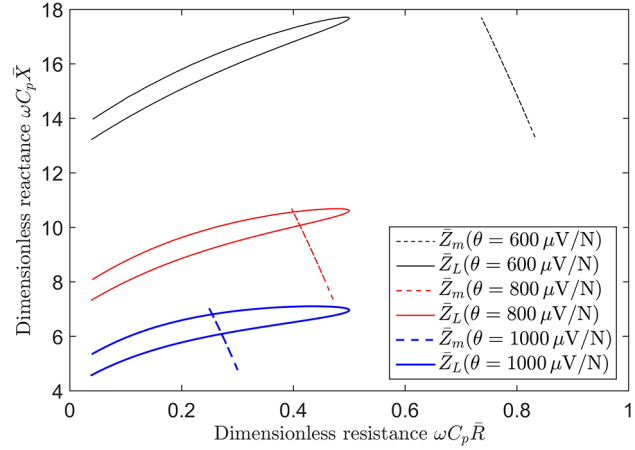


**Figure 11.** Impedance plot of monostable PEH at excitation  $A = 2 \text{ m/s}^2$  with various electromechanical coupling. Corresponding peak power curves are shown in Figure 9(b).

Even though monostable harvesters do not have a single tuning-impedance curve that accounts for all combinations of  $\omega$  or  $R$  as linear harvesters do, the impedance plot still offers interesting insights on their power behaviors, which can still be explained by the same impedance plot concepts applied to linear harvesters (Liao, 2019). Figure 11 plots the impedance curves corresponding to the peak power curves with  $\theta = 600, 800$ , and  $1000 \text{ } \mu\text{V/N}$  in Figure 9(b). Since the matched impedance  $\bar{Z}_m$  depends on  $\theta$  as in equation (37), there are three matched impedance curves with one for each  $\theta$  value. As the coupling increases, the matched impedance curve moves to the left. Graphically, as the frequency  $\omega$  increases, the matched impedance point moves from top to bottom on the curve. On the contrary, the “C” shaped curve is the tuning load impedance  $\bar{Z}_L$  curve, which is defined by equation (38). Figure 9(b) shows that as the load resistance increases, initially the peak power frequency decreases and then increases. On the impedance plot, this corresponds to a clockwise movement on the  $\bar{Z}_L$  curve, noting that the vertical axis is associated with the effective stiffness of the system (Liao, 2019) and an upward movement is associated with a decrease in stiffness, resulting in a lower natural frequency. In addition, Figure 9(b) shows that the system of  $\theta = 600 \text{ } \mu\text{V/N}$  is weakly coupled and the systems of  $\theta = 800$  and  $1000 \text{ } \mu\text{V/N}$  are strongly coupled. A “visual” explanation is provided by Figure 11, where the  $\bar{Z}_L$  curves of the 800 and  $1000 \text{ } \mu\text{V/N}$  configurations are able to intersect their corresponding  $\bar{Z}_m$  curves, that is, impedance matching. The two intersection locations on the matched curve are paired with the two power limit points on the peak power curve. However, the tuned load and matched impedance curves of the  $600 \text{ } \mu\text{V/N}$  configuration are not able to intersect each other. As a result, the power

limit is not reached and the system is weakly coupled. Finally, the distance between the tuning load impedance and matched impedance points can be used as an indicator of the power level qualifiedly (Liao, 2019), which increases as the distance decreases. As a result of this relationship and the non-monotonously change of the peak power frequency along the load impedance curve, the peak power curve of a strongly coupled monostable harvester has a more complex “ $\infty$ ” shape than that of a linear harvester shown in Figure 9(a).

### 5.3. Effect of coupling and excitation

The study in Section 5.2 shows that the minimum (or critical) couplings to reach the power limit for linear and monostable PEHs are different. For a resistive energy harvesting circuit interface, its critical coupling expression in terms of the mechanical damping ratio has been obtained and the system can be defined as weakly, critically, or strongly coupled based on the following criterion (Liao and Liang, 2018)

$$\begin{cases} k_e^2 < 4\zeta + 4\zeta^2, & \text{Weakly Coupled} \\ k_e^2 = 4\zeta + 4\zeta^2, & \text{Critically Coupled} \\ k_e^2 > 4\zeta + 4\zeta^2, & \text{Strongly Coupled} \end{cases} \quad (39)$$

where the dimensionless effective coupling coefficient is defined as

$$k_e^2 = \frac{\theta^2}{C_p K} \quad (40)$$

To determine the critical coupling for the monostable PEH shunted to a purely resistive load interface circuit, note that the second expression for the reactance component of equation (33) must be zero. Simplifying the expression yields

$$\begin{aligned} & \left( \omega^2 M - K + K_1 - \frac{3}{4} K_3 |r|^2 \right) \\ & \left[ -\theta^2 + C_p \left( \omega^2 M - K + K_1 - \frac{3}{4} K_3 |r|^2 \right) \right] \\ & + C_p C^2 \omega^2 = 0 \end{aligned} \quad (41)$$

which can be rearranged into a quadratic equation in terms of  $\omega^2$

$$\begin{aligned} & \omega^4 M^2 + \omega^2 \left[ -M\theta^2/C_p - 2M \left( K - K_1 + \frac{3}{4} K_3 |r|^2 \right) + C^2 \right] \\ & + \left( K - K_1 + \frac{3}{4} K_3 |r|^2 \right)^2 \\ & + \theta^2/C_p \left( K - K_1 + \frac{3}{4} K_3 |r|^2 \right) = 0 \end{aligned} \quad (42)$$

The discriminant  $\Delta$  of the equation is given by

$$\Delta = [-M\theta^2/C_p + C^2]^2 - 4MC^2 \left( K - K_1 + \frac{3}{4} K_3 |r|^2 \right) \quad (43)$$

and the solution to equation(42) is

$$\omega_{1,2} = \sqrt{\frac{M\theta^2/C_p + 2M \left( K - K_1 + 0.75K_3 |r|^2 \right) - C^2 \pm \sqrt{\Delta}}{2M^2}} \quad (44)$$

Real solutions exist when  $\Delta \geq 0$ , that is

$$M\theta^2/C_p \geq 2C\sqrt{MK} \left( \sqrt{1 - \frac{K_1}{K} + \frac{0.75K_3}{K} |r|^2} \right) + C^2 \quad (45)$$

With some algebraic manipulation, one obtains

$$k_e^2 \geq 4\zeta \left( \sqrt{1 - \frac{K_1}{K} + \frac{0.75K_3}{K} |r|^2} \right) + 4\zeta^2 \quad (46)$$

Similar to linear PEHs, equation (46) gives the realization condition of power limit for a monostable PEH, based on which the power behavior can be classified into three categories

$$\begin{cases} k_e^2 < 4\zeta \left( \sqrt{1 - \frac{K_1}{K} + \frac{0.75K_3}{K} |r|^2} \right) + 4\zeta^2, & \text{Weakly Coupled} \\ k_e^2 = 4\zeta \left( \sqrt{1 - \frac{K_1}{K} + \frac{0.75K_3}{K} |r|^2} \right) + 4\zeta^2, & \text{Critically Coupled} \\ k_e^2 > 4\zeta \left( \sqrt{1 - \frac{K_1}{K} + \frac{0.75K_3}{K} |r|^2} \right) + 4\zeta^2, & \text{Strongly Coupled} \end{cases} \quad (47)$$

It can be seen that if the magnetic interaction induced stiffness  $K_1$  and  $K_3$  are set to be zero, that is, removing the magnets from the system, equation (47) returns to equation (39), the coupling relationship equation of a linear PEH.

From equation (46) it can be seen that for monostable PEHs, the critical coupling efficient depends on not only the intrinsic mechanical damping ratio of the system but also the amplitude of displacement response, and the magnetic force constants. This is different from linear PEHs, whose critical coupling coefficient depends only on the mechanical damping ratio. For illustration purposes, Figure 12 depicts the relationship for a linear PEH between the power peak frequency and the electromechanical coupling as the base excitation acceleration changes. It can be seen that the base acceleration has no influence on the relation of power peaks and electromechanical coupling. As the coupling increases,

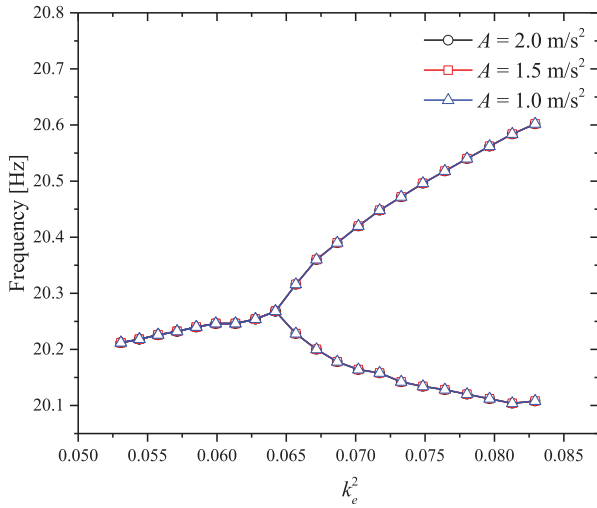
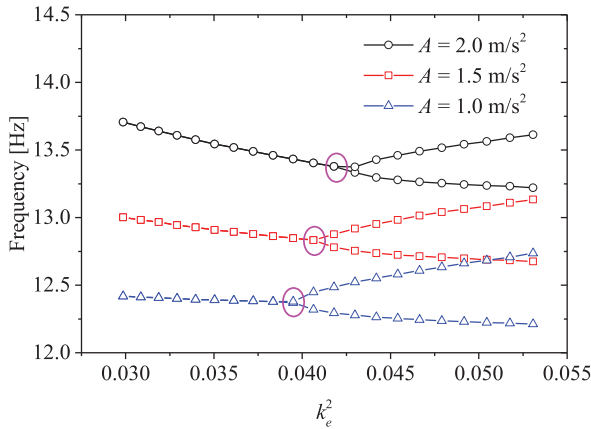


**Figure 12.** Power peak frequency versus coupling coefficient of a linear PEH for various base excitations.

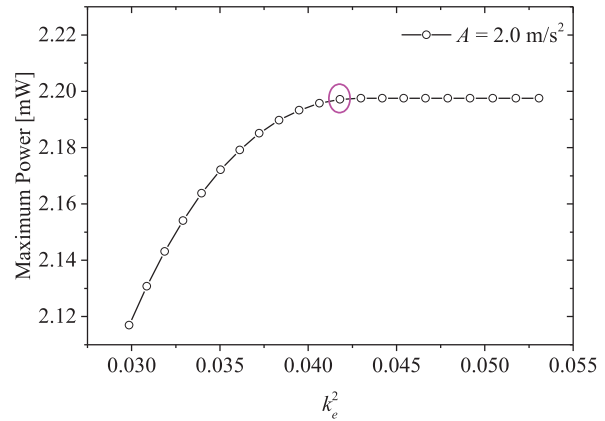
the frequency of the overall power peak increases slowly. However, the power level has not reached the

power limit yet. When the coupling coefficient reaches its critical, a bifurcation is observed, and the power limit is reached. After that, two power limit peaks occur, and one is moving to the higher frequency while the other to the lower frequency.

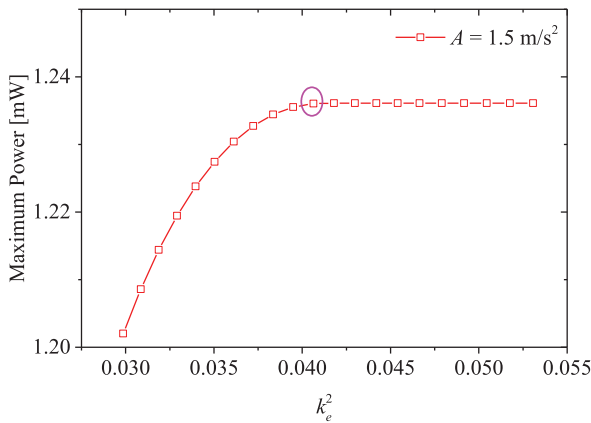
On the contrary, for monostable PEHs, the relationship between the power peak frequency and electromechanical coupling depends on the base excitation as shown in Figure 13(a), where the frequency of the overall power peak is plotted against the coupling coefficient at different base excitation levels. It is revealed that the critical electromechanical coupling for a monostable PEH is significantly reduced when the excitation is relatively low. For example, the critical coupling of the counterpart linear PEH is  $k_e^2 = 0.06422$  while that of monostable PEH is  $k_e^2 = 0.03948$  when  $A = 1 \text{ m/s}^2$ . This can be explained mathematically by noting that in equation (44) the magnetic force constant  $K_1$  makes a negative contribution to the critical coupling while the contribution associated with the constant  $K_3$  is very small under the condition of low-amplitude response, that is,  $r$  is small. Meanwhile, the critical electromechanical coupling is affected by the base excitation and it



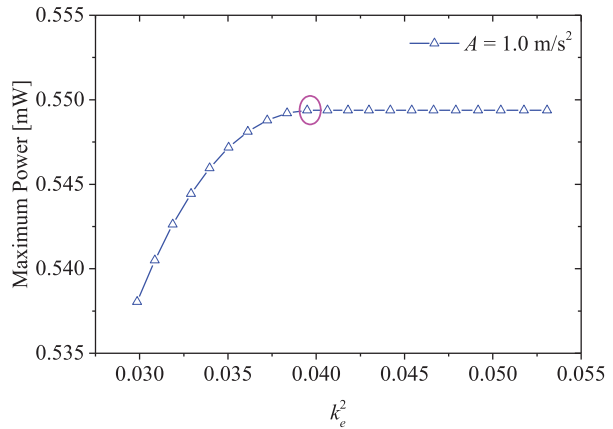
(a)



(b)



(c)



(d)

**Figure 13.** Power limits of a monostable PEH ( $D_0 = 12.25 \text{ mm}$ ): (a) effect of base excitation on the critical electromechanical coupling and (b) to (d) maximum power versus  $k_e^2$ : (b)  $A = 2 \text{ m/s}^2$ , (c)  $A = 1.5 \text{ m/s}^2$ , and (d)  $A = 1 \text{ m/s}^2$ .



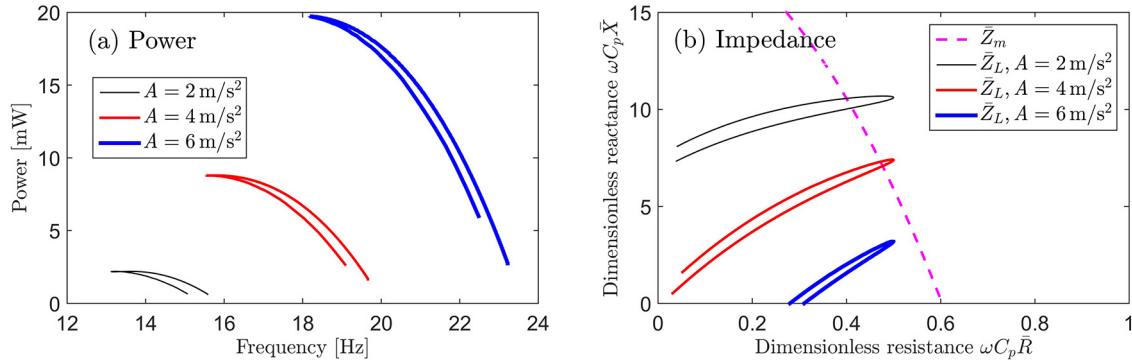


**Figure 14.** (a) Power and (b) impedance plot of a monostable PEH ( $D_0 = 12.25$  mm) subjected to various base excitations.  $\theta = 800$   $\mu\text{V/N}$ .

increases with the level of base excitation. Figure 13(b) to (d) shows how the peak power changes at those different base excitation levels. It can be seen that the power limit increases proportionally with the excitation level. Also noticeable is the difference in critical (or minimum) electromechanical coupling to reach power limit. For  $A = 1, 1.5$ , and  $2$   $\text{m/s}^2$ , the critical coupling coefficients are  $0.03948$ ,  $0.04064$ , and  $0.04181$ , respectively. This result agrees with the conclusion drawn from equation (44) that the critical coupling should increase as the structural response  $r$  increases. In all, it is concluded that although the power limits of a linear PEH and a monostable PEH are the same, the required electromechanical coupling to reach power limit could be significantly reduced at low excitation level by introducing the stiffness nonlinearity through magnetic force, which is desirable for vibration energy harvesting systems under weak coupling conditions.

Another perspective of the excitation effect on coupling is provided by Figure 14, where the peak power curves at various base excitation levels are presented in Figure 14(a) and their corresponding load and matched impedance curves are plotted in Figure 14(b). As mentioned previously, a weakly coupled PEH could become a strongly coupled monostable PEH at low excitation level. However, as the excitation level increases, the response becomes larger and consequently, the critical coupling increases too. As a result, a strongly coupled system could become weakly coupled if the excitation is large enough. This is graphically illustrated in Figure 14(b). The system is strongly coupled at excitation  $A = 2$  and  $4$   $\text{m/s}^2$ , but it becomes weakly coupled at  $A = 6$   $\text{m/s}^2$ .

#### 5.4. Effect of magnetic field

As discussed in Section 5.2.2, the addition of magnets to a linear PEH is equivalent to adding an auxiliary

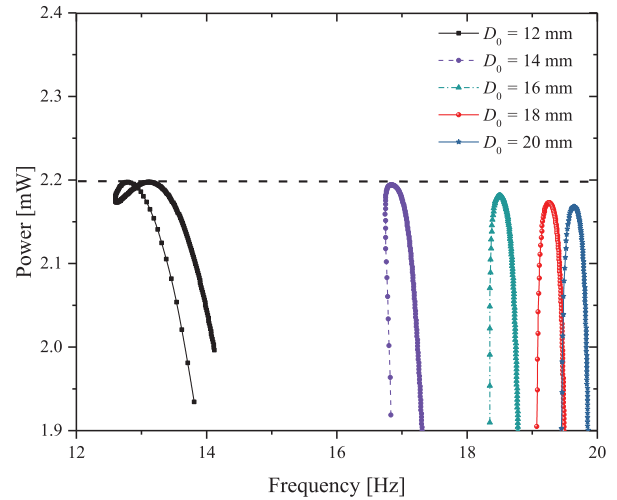


**Figure 15.** Effect of magnet distance  $D_0$  on the maximum power of a monostable PEH when  $k_e^2 = 0.05$ ,  $A_0 = 2$   $\text{m/s}^2$ .

nonlinear stiffness element in the mechanical domain, and a nonlinear capacitor in the electrical domain. Although it does not change the overall power limit of the system, it does have a significant effect on the overall effective stiffness and the electromechanical coupling condition. Physically, the nonlinearity of the system is induced by the magnetic force between the magnets. The effect of magnetic field on the system in the form of the distance between the magnets is studied in this section. By varying the magnet distance, Figure 15 plots the power peaks of a monostable PEH at a fixed coupling coefficient  $k_e^2 = 0.05$ .

There are some important observations that can be made. First, as the distance decreases, the power peak curve shifts to the lower frequency. This can be explained by noting that the additional nonlinear stiffness as given in equation (21) is negative if the

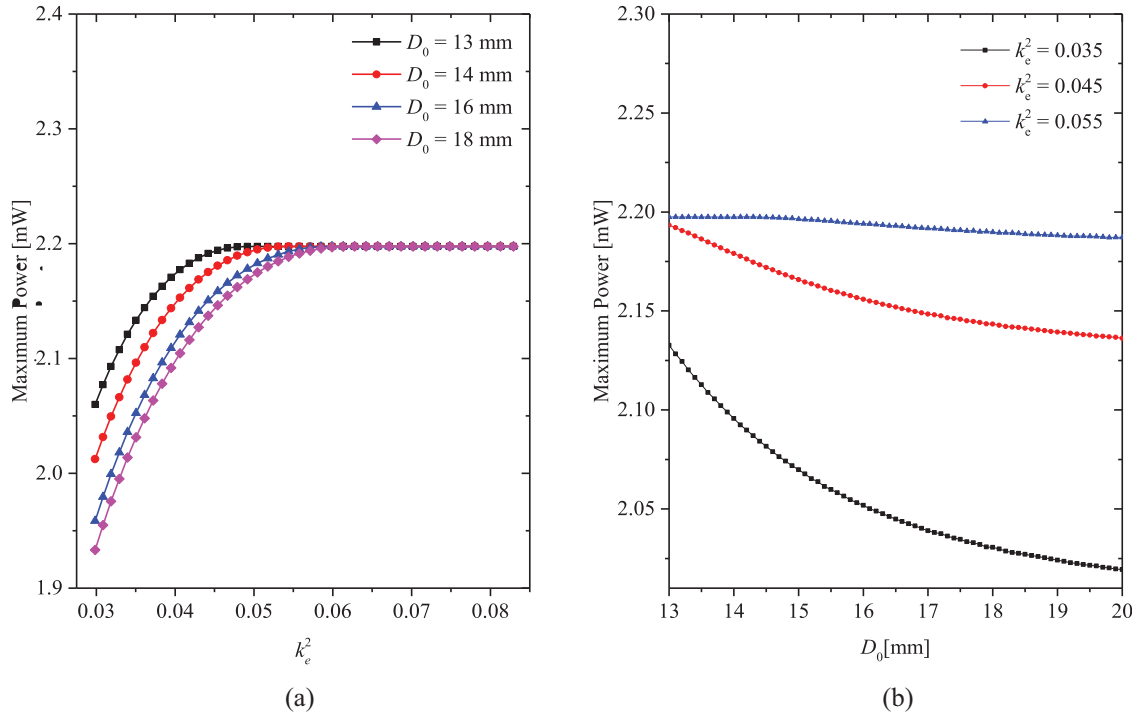


**Figure 16.** Maximum power of a monostable PEH for different  $D_0$  and  $k_e^2$  ( $A_0 = 2 \text{ m/s}^2$ ): (a) effect of magnetic distance and (b) effect of electromechanical coupling.

structural response is not significantly large, and the magnetic force constants  $K_1$  and  $K_3$  defined in equation (5) increase as the magnet distance decreases, resulting in a greater reduction in the overall effective stiffness of the system. Second, it appears that the overall power level increases as the distance decreases before the power saturates. This effect is further illustrated in Figure 16, where the overall maximum power is plotted against the coupling coefficient and magnetic distance. Under the weak electromechanical coupling condition, a stronger nonlinearity leads to a higher maximum power, which validates the experimental observation by Stanton et al. (2009). The power increase can be explained by the fact that the critical coupling (required to reach the power limit) decreases as the magnet distance decreases, as shown in equation (47). This change in critical coupling is better illustrated in Figure 17. The critical coupling, that is, the bifurcation point, increases with the decrease of the magnet distance. Third, Figure 17 shows how the power peak frequency moves as a result of the increased coupling for various magnet distances. For large distances, for example, 16 and 18 mm, the power peak frequency increases before reaching the power limit, which is very similar to that of the linear PEH. This is expected because that the magnetic force is still not strong enough to have a substantial effect on the system due to the far distance. On the contrary, for a small  $D_0$ , such as 13 and 14 mm, the power peak frequency decreases before reaching the power limit. This is a result of a stronger nonlinearity

introduced by a shorter distance. Finally, but very importantly, Figures 15 and 16(a) show that the power limit of the system is the same regardless of the magnet distance and electromechanical coupling, which affirms the conclusion drawn in Section 5.1 that the monostable PEH has the same power limit as that of the linear PEH.

## 6. Conclusion

To ascertain the inherent mechanism of power improvement of nonlinear PEHs, this work investigates the maximum power and power limit of monostable PEHs as an example. For this purpose, an equivalent linearization method based on the harmonic balance technique is proposed to linearize the nonlinear term in the system governing equation and obtain the equivalent circuit of monostable PEHs. Then, the impedance matching technique is applied to determine the power limit and critical coupling of the system. Several important conclusions are drawn as follows:

1. The power limit of a monostable PEH is the same with that of its linear counterpart, regardless of the degree of nonlinearity and level of external excitations.
2. Adding magnets to a linear PEH to make it monostable is equivalent to adding a nonlinear capacitor into the electrical energy harvesting circuit interface of the linear PEH. This

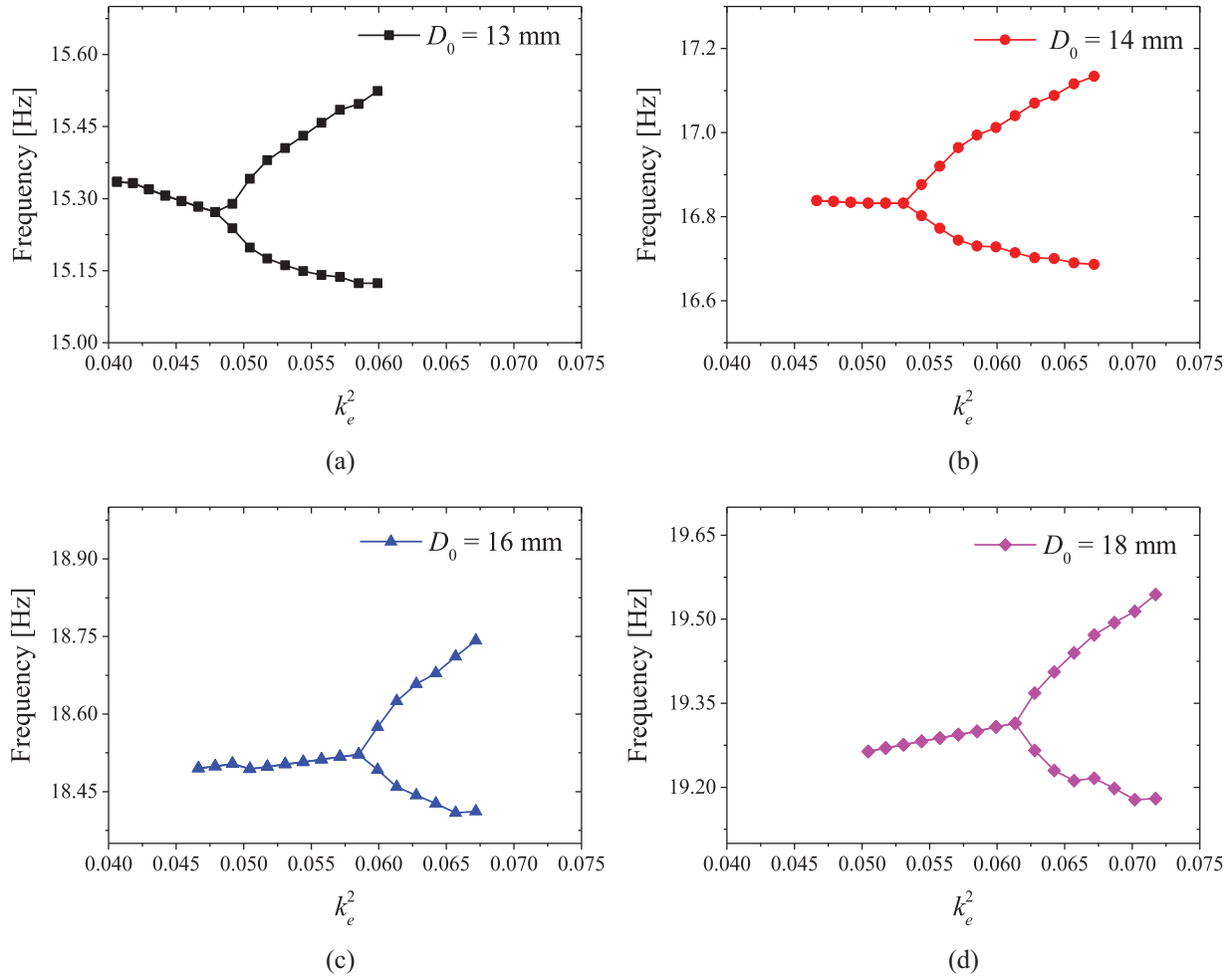


**Figure 17.** Relationships between power peak frequency and electromechanical coupling of a monostable PEH for different  $D_0$  ( $A_0 = 2 \text{ m/s}^2$ ). (a)  $D_0 = 13$  mm; (b)  $D_0 = 14$  mm; (c)  $D_0 = 16$  mm; (d)  $D_0 = 18$  mm.

auxiliary capacitor changes or tunes the electrical impedance of the linear PEH but does not change the power limit since it is a reactive component.

3. The critical electromechanical coupling of monostable PEHs depends on the external excitation, nonlinear stiffness, and damping ratio. The critical coupling of monostable PEH is much lower than that of its linear counterpart when the base excitation is small, which means that the nonlinearity is an effective way to reduce the requirement of piezoelectric materials and improve the electromechanical conversion efficiency.
4. The critical coupling can be decreased by reducing the magnetic distance, resulting in an increase in the output power before reaching its power limit.
5. The impedance plot built on the relationship between the source and load impedances is still

a valuable tool to understand and analyze power behavior of monostable PEHs.

While the discussion is focused on monostable PEHs connected with a resistive interface circuit, the approach and results can be extended to other types of interface circuits as well.

#### Declaration of conflicting interests


The author(s) declared no potential conflicts of interest with respect to the research, authorship, and/or publication of this article.


#### Funding

The author(s) disclosed receipt of the following financial support for the research, authorship, and/or publication of this article: This study was supported by the New Staff Foundation of Nanjing University of Aeronautics and Astronautics (Grant No. 1001-YAH18051), Natural Science

Foundation of China (Grant No. 11672237), and Natural Science Foundation of Jiangsu Province (Grant No. BK20190379).

## ORCID iDs

Yabin Liao  <https://orcid.org/0000-0003-4054-5219>

Lihua Tang  <https://orcid.org/0000-0001-9031-4190>

## References

- Brenes A, Morel A, Juillard J, et al. (2020) Maximum power point of piezoelectric energy harvesters: a review of optimality condition for electrical tuning. *Smart Materials and Structures* 29: 033001.
- Chen L and Jiang W (2015) Internal resonance energy harvesting. *Journal of Applied Mechanics* 82: 031004.
- Cottone F, Vocca H and Gammaitoni L (2009) Nonlinear energy harvesting. *Physical Review Letters* 102: 080601.
- Daqaq MF, Masana R, Erturk A, et al. (2014) On the role of nonlinearities in vibratory energy harvesting: a critical review and discussion. *Applied Mechanics Reviews* 66: 040801.
- Erturk A and Inman DJ (2011a) Broadband piezoelectric power generation on high-energy orbits of the bistable Duffing oscillator with electromechanical coupling. *Journal of Sound and Vibration* 330: 2339–2353.
- Erturk A and Inman DJ (2011b) *Piezoelectric Energy Harvesting*. John Wiley & Sons.
- Hagood NW, Chung WH and Von Flotow A (1990) Modeling of piezoelectric actuator dynamics for active structural control. *Journal of Intelligent Material Systems and Structures* 1: 327–354.
- Lan C, Tang L and Harne RL (2018a) Comparative methods to assess harmonic response of nonlinear piezoelectric energy harvesters interfaced with AC and DC circuits. *Journal of Sound and Vibration* 421: 61–78.
- Lan C, Tang L, Qin W, et al. (2018b) Magnetically coupled dual-beam energy harvester: benefit and trade-off. *Journal of Intelligent Material Systems and Structures* 29: 1216–1235.
- Liang J and Liao WH (2012) Impedance modeling and analysis for piezoelectric energy harvesting systems. *IEEE/ASME Transactions on Mechatronics* 17: 1145–1157.
- Liao Y (2019) Analysis of power and efficiency of piezoelectric vibration energy harvesters through an impedance plot. *Journal of Intelligent Material Systems and Structures* 30: 3036–3055.
- Liao Y and Liang J (2018) Maximum power, optimal load, and impedance analysis of piezoelectric vibration energy harvesters. *Smart Materials and Structures* 27: 075053.
- Liao Y and Liang J (2019) Unified modeling, analysis and comparison of piezoelectric vibration energy harvesters. *Mechanical Systems and Signal Processing* 123: 403–425.
- Liao Y and Sodano HA (2008) Model of a single mode energy harvester and properties for optimal power generation. *Smart Materials and Structures* 17: 065026.
- Liao Y and Sodano HA (2009) Optimal parameters and power characteristics of piezoelectric energy harvesters with an RC circuit. *Smart Materials and Structures* 18: 045011.
- Liu H, Lee C, Kobayashi T, et al. (2012) Investigation of a MEMS piezoelectric energy harvester system with a frequency-widened-bandwidth mechanism introduced by mechanical stoppers. *Smart Materials and Structures* 21: 035005.
- Liu H, Zhong J, Lee C, et al. (2018) A comprehensive review on piezoelectric energy harvesting technology: materials, mechanisms, and applications. *Applied Physics Reviews* 5: 041306.
- McInnes C, Gorman D and Cartmell MP (2008) Enhanced vibrational energy harvesting using nonlinear stochastic resonance. *Journal of Sound and Vibration* 318: 655–662.
- Renno JM, Daqaq MF and Inman DJ (2009) On the optimal energy harvesting from a vibration source. *Journal of Sound and Vibration* 320: 386–405.
- Shu YC and Lien IC (2006a) Analysis of power output for piezoelectric energy harvesting systems. *Smart Materials and Structures* 15: 1499.
- Shu YC and Lien IC (2006b) Efficiency of energy conversion for a piezoelectric power harvesting system. *Journal of Micromechanics and Microengineering* 16: 2429.
- Stanton SC, McGehee CC and Mann BP (2009) Reversible hysteresis for broadband magnetopiezoelectric energy harvesting. *Applied Physics Letters* 95: 174103.
- Stanton SC, Owens BA and Mann BP (2012) Harmonic balance analysis of the bistable piezoelectric inertial generator. *Journal of Sound and Vibration* 331: 3617–3627.
- Su W, Zu J and Zhu Y (2014) Design and development of a broadband magnet-induced dual-cantilever piezoelectric energy harvester. *Journal of Intelligent Material Systems and Structures* 25: 430–442.
- Tao K, Yi H, Tang L, et al. (2019) Piezoelectric ZnO thin films for 2DOF MEMS vibrational energy harvesting. *Surface and Coatings Technology* 359: 289–295.
- Wei CF and Jing XJ (2017) A comprehensive review on vibration energy harvesting: modelling and realization. *Renewable & Sustainable Energy Reviews* 74: 1–18.
- Williams C and Yates RB (1996) Analysis of a micro-electric generator for microsystems. *Sensors and Actuators A: Physical* 52: 8–11.
- Wu Y, Qiu J, Zhou S, et al. (2018) A piezoelectric spring pendulum oscillator used for multi-directional and ultra-low frequency vibration energy harvesting. *Applied Energy* 231: 600–614.
- Xiong L, Tang L, Liu K, et al. (2018) Broadband piezoelectric vibration energy harvesting using a nonlinear energy sink. *Journal of Physics D: Applied Physics* 51: 185502.
- Xu J and Tang J (2017) Modeling and analysis of piezoelectric cantilever-pendulum system for multi-directional energy harvesting. *Journal of Intelligent Material Systems and Structures* 28: 323–338.
- Yang Z, Erturk A and Zu J (2017) On the efficiency of piezoelectric energy harvesters. *Extreme Mechanics Letters* 15: 26–37.
- Yang Z, Zhou S, Zu J, et al. (2018) High-performance piezoelectric energy harvesters and their applications. *Joule* 2(4): 642–697.
- Yang Z, Zhu Y and Zu J (2015) Theoretical and experimental investigation of a nonlinear compressive-mode energy harvester with high power output under weak excitations. *Smart Materials and Structures* 24(2): 025028.

- Yung KW, Landecker PB and Villani DD (1998) An analytic solution for the force between two magnetic dipoles. *Physical Separation in Science and Engineering* 9: 39–52.
- Zhao LY and Yang YW (2018) An impact-based broadband aeroelastic energy harvester for concurrent wind and base vibration energy harvesting. *Applied Energy* 212: 233–243.
- Zhou S and Zuo L (2018) Nonlinear dynamic analysis of asymmetric tristable energy harvesters for enhanced energy harvesting. *Communications in Nonlinear Science and Numerical Simulation* 61: 271–284.

## Appendix I

To obtain the approximate analytical solutions of this monostable PEH, HBM has been employed in this section. First, assuming the appropriate solutions have the following form

$$\begin{cases} w(t) = a_1(t) \sin(\omega t) + b_1(t) \cos(\omega t) \\ V(t) = a_2(t) \sin(\omega t) + b_2(t) \cos(\omega t) \\ \dot{w}(t) = [\dot{a}_1(t) - \omega b_1(t)] \sin(\omega t) \\ \quad + [\omega a_1(t) + \dot{b}_1(t)] \cos(\omega t) \\ \dot{V}(t) = [\dot{a}_2(t) - \omega b_2(t)] \sin(\omega t) \\ \quad + [\omega a_2(t) + \dot{b}_2(t)] \cos(\omega t) \\ \ddot{w}(t) = [-\omega^2 a_1(t) - 2\omega \dot{b}_1(t)] \sin(\omega t) \\ \quad + [2\omega \dot{a}_1(t) - \omega^2 b_1(t)] \cos(\omega t) \end{cases} \quad (48)$$

Substituting equation (48) into the governing equation (6), neglecting the higher harmonics and balancing the terms of  $\sin(\omega t)$  and  $\cos(\omega t)$ , one obtains

$$\begin{cases} -M\omega^2 a_1(t) - C\omega b_1(t) + (K - K_1)a_1(t) - \theta a_2(t) \\ \quad + \frac{3}{4}K_3(a_1^3(t) + a_1(t)b_1^2(t)) = 2M\omega \dot{b}_1(t) - C\dot{a}_1(t) \\ -M\omega^2 b_1(t) + C\omega a_1(t) + (K - K_1)b_1(t) - \theta b_2(t) \\ \quad + \frac{3}{4}K_3(b_1^3(t) + b_1(t)a_1^2(t)) - DA = -2M\omega \dot{a}_1(t) \\ \quad - C\dot{b}_1(t) \\ \frac{a_2(t)}{R_L} - \omega C_p b_2(t) - \omega \theta b_1(t) = -C_p \dot{a}_2(t) - \theta \dot{a}_1(t) \\ \frac{b_2(t)}{R_L} + \omega C_p a_2(t) + \omega \theta a_1(t) = -C_p \dot{b}_2(t) - \theta \dot{b}_1(t) \end{cases} \quad (49)$$

In the steady state, all time derivatives vanish so that equation (49) can be simplified as

$$\begin{cases} -M\omega^2 a_1 - C\omega b_1 + (K - K_1)a_1 - \theta a_2 \\ \quad + \frac{3}{4}K_3(a_1^3 + a_1 b_1^2) = 0 \\ -M\omega^2 b_1 + C\omega a_1 + (K - K_1)b_1 - \theta b_2 \\ \quad + \frac{3}{4}K_3(b_1^3 + b_1 a_1^2) - DA = 0 \\ \frac{a_2}{R_L} - \omega C_p b_2 - \omega \theta b_1 = 0 \\ \frac{b_2}{R_L} + \omega C_p a_2 + \omega \theta a_1 = 0 \end{cases} \quad (50)$$

Solving equation (50) gives the coefficients ( $a_1$ ,  $a_2$ ,  $b_1$ ,  $b_2$ ) and the responses of this monostable PEH. The solutions are given as

$$\begin{aligned} r^2 \left[ \left( -\omega^2 M + K - K_1 + \frac{3}{4}K_3 r^2 + \frac{C_p(\theta R_L \omega)^2}{(C_p R_L \omega)^2 + 1} \right)^2 \right. \\ \left. + \omega^2 \left( \frac{C + R_L \theta^2}{(C_p R_L \omega)^2 + 1} \right)^2 \right] = (DA)^2 \end{aligned} \quad (51)$$

where  $r = \sqrt{a_1^2 + b_1^2}$  is the amplitude of displacement,  $A$  is the magnitude of base acceleration, and  $\omega$  is the frequency of base acceleration. When given the frequency and magnitude of base excitation, the amplitude of displacement can be obtained from equation (50). To determine the stability of the solutions obtained from equation (50), equation (49) is cast into the form  $\mathbf{P}\dot{\mathbf{w}} = \mathbf{Q}(\mathbf{w})$ , where vector  $\mathbf{w}$  is defined by  $\mathbf{w} = [a_1, b_1, a_2, b_2]^T$ . Thus,  $\dot{\mathbf{w}} = \mathbf{P}^{-1}\mathbf{Q}(\mathbf{w})$ . The Jacobian matrix can be determined by

$$\mathbf{H} = \frac{\partial(\mathbf{P}^{-1}\mathbf{Q}(\mathbf{w}))}{\partial(\mathbf{w})} \quad (52)$$

The solution of this monostable PEH is stable only if all the eigenvalues of the Jacobian matrix  $\mathbf{H}$  are negative real numbers. Meanwhile, the amplitude of output voltage and output power are

$$\begin{cases} V = \frac{\theta R_L \omega}{\sqrt{(C_p R_L \omega)^2 + 1}} r \\ P = \frac{(\theta \omega)^2 R_L}{(C_p R_L \omega)^2 + 1} r^2 \end{cases} \quad (53)$$